ASIA-PACIFIC SOLAR RESEARCH CONFERENCE

Peer Reviewed
2017 Solar Research Conference

Matthew J. Emes

Experimental Investigation of the Wind Loads on Heliostats

Matthew J. Emes, Jeremy S. Yu, Azadeh Jafari, Farzin Ghanadi and Maziar Arjomandi

School of Mechanical Engineering, The University of Adelaide, Adelaide, South Australia 5005, Australia

E-mail: matthew.emes@adelaide.edu.au

Abstract

Concentrating solar thermal (CST) power tower (PT) is an emerging renewable technology for large-scale electricity production, however the main limitation is their significantly larger levelised cost of electricity (LCOE) relative to base load energy systems. One opportunity to lower the LCOE is to reduce the capital cost of heliostats through optimisation of the maximum wind loads during operation at different elevation and azimuth angles and during high-wind conditions when aligned parallel to the ground in the stow position.

Wind tunnel experiments were carried out to measure the forces on thin flat plates of various sizes at a range of elevation angles, azimuth angles and heights in a simulated part-depth atmospheric boundary layer (ABL). Peak wind load coefficients on heliostats in operating and stow positions are significantly dependent on the critical scaling parameters of the heliostat and the turbulence characteristics approaching them. The largest load coefficients on operating and stowed heliostats occurred at an azimuth angle $\beta = 0°$ with the heliostat facet aligned with the incident flow. Peak drag coefficients on operating heliostats increased with increasing elevation angle of the heliostat mirror ($\alpha > 0°$) to a maximum in the normal position ($\alpha = 90°$). The effect of increasing the approaching turbulence intensity I_u from 2% to 8% was more significant on the peak drag loads compared to the mean drag loads with increasing α. The lift force and hinge moment coefficients on a stowed heliostat ($\alpha = 0°$) increased linearly with increasing turbulence intensity $I_u > 10\%$ and an increasing ratio of integral length scale to heliostat chord length L_u^x/c in stow position ($\alpha = 0°$). Furthermore, the peak wind loads on a stowed heliostat decreased by up to 40% when the ratio of elevation axis height to chord length of the heliostat mirror, H/c, was reduced to less than 0.5. Optimisation of the design wind loads on isolated heliostats in operation and stow positions to the characteristics of the turbulence approaching them can lead to reductions in the cost of manufacturing the heliostat components.

1. Introduction

Current energy systems, based primarily on the combustion of fossil fuels, are unsustainable in the long term, so that a transition to an environmentally-sustainable energy system with the integration of renewable energy sources is necessary (Hernández-Moro and Martínez-Duart 2012). Concentrating solar thermal (CST) is one of the most promising renewable technologies capable of large scale electricity production (Hinkley *et al.* 2013). A CST system operates by focusing direct solar radiation to obtain higher energy densities and thus an improved Carnot efficiency at higher temperatures. Heat collected in the receiver is typically used to heat a working fluid to generate supercritical steam that drives a turbine for electricity generation (IRENA 2015). Parabolic trough systems are the most commercially-deployed CST technology, however power tower (PT) systems have been identified as an emerging concept that can operate at higher concentration ratios and higher working fluid temperatures than parabolic troughs, thus allowing for higher power cycle efficiency (IEA-ETSAP and IRENA 2013). Although the intermittency of solar irradiation is a practical limitation of CST systems, PT plants can be deployed with thermal energy storage or as a hybrid system with existing fossil fuel power plants for a base-line power supply (Kolb *et al.* 2011; Hinkley *et al.* 2013).

The main limitation of PT systems is their significantly larger levelised cost of electricity (LCOE), in the range of 0.15-0.19 USD/kWh in 2015 (IRENA 2015), compared to base-load energy systems such as fossil fuel power plants in the range of 0.06-0.13 USD/kWh in 2011 (IRENA 2013). To reduce the LCOE of PT systems there is a need to lower the capital cost of a PT plant, of which the largest cost is the heliostat field, with an estimated contribution of between 40% and 50% (Kolb *et al.* 2007; Hinkley *et al.* 2013; Coventry and Pye 2014; IRENA 2015). Government-funded initiatives that support the research and development of CST systems to make them competitive with base-load energy rates include the SunShot Initiative by the Department of Energy (DOE) in the USA, with a goal LCOE of 0.06 USD/kWh by 2020 (Kolb *et al.* 2011), and the Australian Solar Thermal Research Initiative (ASTRI) targeting a LCOE of 0.12 AUD/kWh by 2020. Currently, the total installed cost of a 150 MW PT plant is 5700 USD/kW (IRENA 2015), and the cost of the heliostat field for high production rates in 2013 was estimated to be US150-200/m^2 (Coventry *et al.* 2013). The LCOE of a conventional molten-salt receiver PT plant was estimated by NREL (Mehos *et al.* 2016) to be 0.14 USD/kWh in 2015, but this could be further reduced to 0.1 USD/kWh with near-term advanced heliostats at \$97/m^2 in a 2017 tower configuration (Mehos *et al.* 2017). The total cost of PT plants is projected to be reduced by 37% to 3600 USD/kW by 2025, compared with a projected 33% reduction in parabolic troughs (IRENA 2015). The largest reduction of 24% in the cost of the heliostat field, to less than USD120/m^2, is expected to be achieved through the optimisation of the structural design of heliostats to wind loading. For example, lowering the design wind speed for stowing the heliostat from 15 m/s to 10 m/s can reduce the heliostat cost by 34% (Emes *et al.* 2015). Furthermore, the stiffness of a concrete pylon is preferred in contemporary heliostat designs (Pfahl *et al.* 2017a), however the lowering of the heliostat mirror using a spindle drive to the ground in stow during high-wind conditions can reduce the wind load requirements and the cost of a cantilever-sandwich heliostat (Pfahl *et al.* 2017b). Hence, the aim of this paper is to investigate the effect of the critical scaling parameters of the heliostat and the turbulence characteristics in the ABL on the peak wind load coefficients on heliostats in operating and stow positions.

2. Experimental Method

2.1. Wind Tunnel Setup

Experimental measurements were taken in a closed-return wind tunnel at the University of Adelaide. Figure 1 shows the test section of the tunnel with a development length of 17 m and a cross-section expanding to 3 m × 3 m to allow for a pressure gradient resulting from growth of the boundary layer. The tunnel can be operated at speeds of up to 20 m/s with a low level of turbulence intensity, ranging between 1% and 3%. Accurate representation of a part-depth ABL in the wind tunnel is required to replicate similar turbulence properties that heliostats are exposed to in the lower surface layer of the ABL, including a logarithmic mean velocity profile. It is generally accepted that the most effective wind tunnel simulation of the ABL is obtained when a flow passes over a rough surface producing a natural-growth boundary layer (De Bortoli *et al.* 2002). The most commonly-used passive devices include spires to generate turbulent mixing through separation of flow around their edges, fence barriers to increase the height of the boundary layer and floor roughness to develop the velocity deficit near the ground (Counihan 1973; Cook 1978). Two different triangular spire designs and timber roughness blocks are shown in Table 1. These dimensions were derived following a theoretical design method outlined by Irwin (1981) such that the height h, base width b and depth d of the spires could be determined based on the desired power law profile with exponent α of 0.2 and boundary layer thickness δ of 1.2 m. Velocity measurements for the two configurations of spire and roughness in Table 1 were taken at different heights using a multi-hole pressure probe and a traverse. The operating conditions of the tunnel were a freestream velocity $U_\infty = 11$ m/s and Reynolds number $Re_\infty = U_\infty \delta / \nu = 8.8{\times}10^5$.

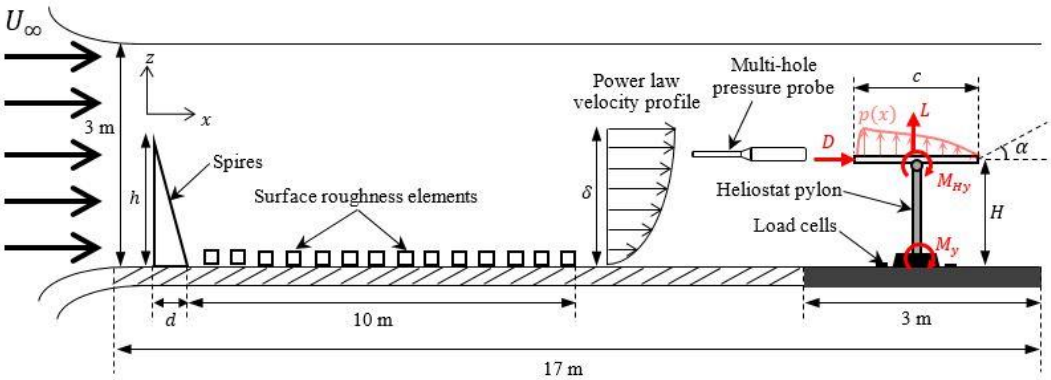

Figure 1. Schematic of the experimental setup for generation of the ABL in the wind tunnel and force measurements on a scale-model heliostat.

Table 1. Dimensions and characteristics of spires and roughness elements

Configuration	Spire height $\boldsymbol{h}$ (m)	Spire base width $\boldsymbol{b}$ (m)	Spire depth $\boldsymbol{d}$ (m)	Roughness width $\boldsymbol{R_b}$ (m)	Roughness height $\boldsymbol{R_h}$ (m)
SR1	1.3	0.155	0.34	0.09	0.045
SR2	1.4	0.2	0.74	0.09	0.045

2.2. Turbulence Characteristics of the Simulated ABL

2.2.1. Velocity and Turbulence Intensity Profiles

Figure 2(a) and (b) show the mean velocity and turbulence intensity profiles, respectively, of the two spire and roughness configurations in Table 1. The mean velocity profiles generated by SR1 are within a maximum error of ±5% of power law ($\alpha = 0.12$) and log law ($z_0 = 0.001$ m) velocity profiles at an ABL model scale of 1:150. The turbulence intensities generated by SR1 are within ±2% of Engineering Sciences Data Unit (1985) data for a neutral ABL with a mean wind speed of 10 m/s at a 10 m height, surface roughness height $z_0 = 0.001$ m and boundary layer thickness $\delta = 350$ m. The mean velocity profile generated by SR2 is close to linear in the part-depth simulated ABL and the turbulence intensity profile is well approximated by the log law profile with surface roughness height $z_0 = 0.015$ m. Hence, the two spire and roughness configurations, SR1 and SR2, can be used to investigate the effect of turbulence intensity on the peak wind loads on the heliostat mirror that was stowed at a range of heights ($0.3 < z/\delta < 0.5$) indicated by the shaded region in Figure 2.

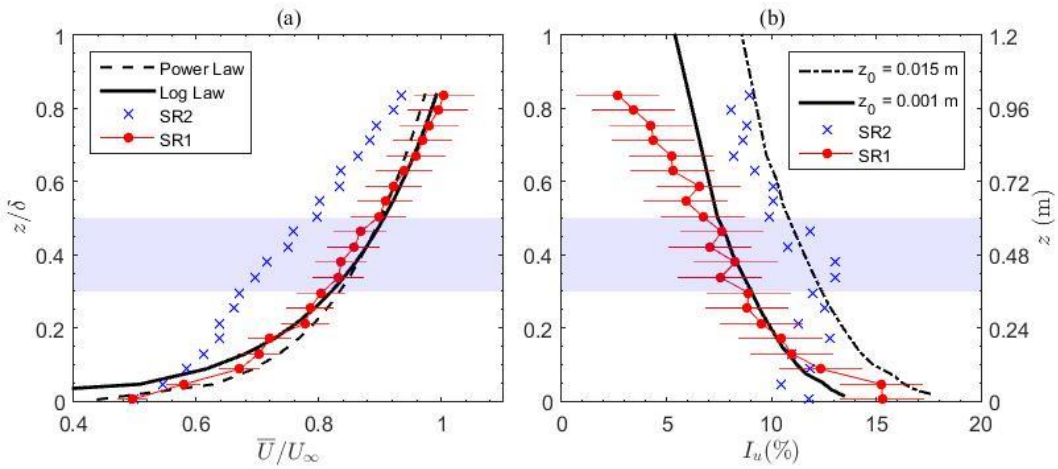

Figure 2. (a) Mean velocity profiles of the two spire configurations compared with the power law and log law profiles of a low-roughness terrain; (b) Longitudinal turbulence intensity profiles compared with the ESDU 85020 (1985) profiles of two different terrain roughness. The shaded area indicates the heights at which the central elevation axis of the heliostat mirror was positioned.

2.2.2. Power Spectra and Integral Length Scales

Figure 3(a) presents the variation of the longitudinal integral length scale $L_u^x = \overline{U}\int_0^{\tau_0} R_u(\tau)\,d\tau$, calculated to the first-zero crossing τ_0 of the autocorrelation function R_u, with non-dimensional height in the ABL ($\delta = 1.2$ m) for SR1 and SR2 to approximate the sizes of the largest vortices approaching the model-scale heliostat. The values of L_u^x show considerable scatter at all heights and are approximately double those measured by Farell and Iyengar (1999) at the same height ($z = 0.6$ m) in an ABL with the same thickness, as shown by the filled data points in Figure

3(a). At the shaded range of heights ($0.3 < z/\delta < 0.5$) where the central elevation axis of the stowed heliostat mirror is positioned, L_u^x varies from 1.6 m to 2 m for SR1 and from 1.9 m to 2.5 m for SR2. This indicates that the largest vortices approaching the stowed heliostat using SR2 were on average 21% larger and as much as double the size of those produced using SR1 in the current study. The predicted L_u^x by ESDU 85020 over-estimated L_u^x by 40% for SR1 and by 17% for SR2 on average over the range of heights ($0.3 < z/\delta < 0.5$). Overall, the values of L_u^x calculated for SR1 and SR2 are below the stated ±8% error of the ESDU 85020 correlations, however this is expected because of the limitation of producing the largest length scales of the ABL in a wind tunnel. Hence, the values of L_u^x for SR1 and SR2 are considered reasonable for wind-load analysis within the highlighted range of heights of the stowed heliostat.

Figure 3(b) compares the non-dimensional power spectra in the longitudinal direction fS_u/σ_u^2 as a function of non-dimensional frequency $fL_u^x/\overline{U}$, at a non-dimensional height $z/\delta = 0.5$ for SR1 and SR2 in the current study, with the fitted von Karman spectrum reported by Farell and Iyengar (1999). The spectral peaks are reflected by integral length scales L_u^x increasing from 0.8 m to 2 m and 2.5 m for SR1 and SR2, respectively, as indicated by the three filled data points at $z/\delta = 0.5$ in Figure 3(a). The spectral peaks corresponding to these values of L_u^x are shifted from 5 Hz to the lower frequencies of 2 Hz and 1 Hz for SR1 and SR2, respectively. Although the low-frequency region of the full-scale turbulent power spectra cannot be replicated in boundary layer wind tunnel experiments (Banks 2011; Pfahl *et al.* 2015), velocity fluctuations measured at the frequencies corresponding to the peak values of the power spectra (Figure 3(b)) were considered sufficient for the calculation of longitudinal integral length scales L_u^x to provide a measure of the largest eddies in the flow.

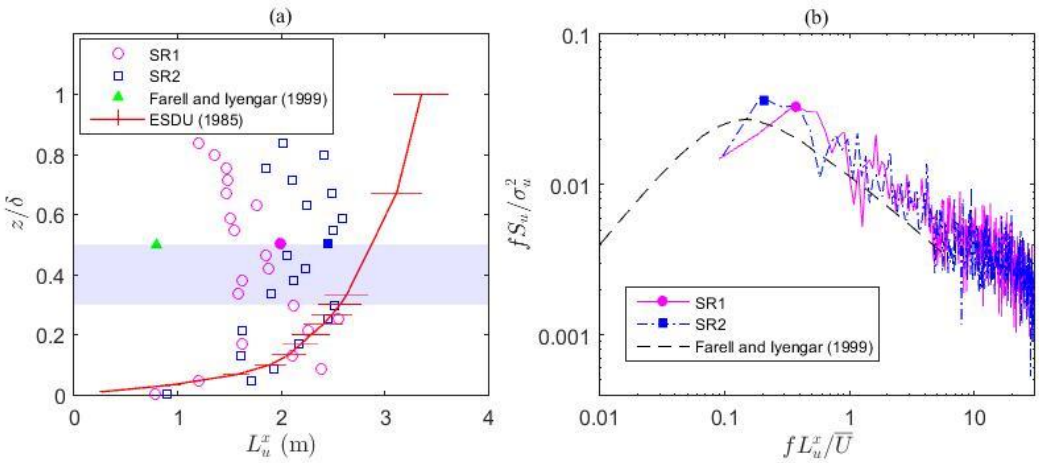

Figure 3. (a) Longitudinal integral length scale profiles of SR1 and SR2 compared with the Engineering Sciences Data Unit (1985) profile for $z_0 = 0.015$ m with an assumed ABL model scale of 1:150 and an experimental study by Farell and Iyengar (1999) at $z/\delta = 0.5$ for a simulated ABL ($\delta = 1.2$ m). The shaded area indicates the heights at which the heliostat mirror was stowed. (b) Longitudinal power spectra of turbulence generated by SR1 and SR2 compared with a von Karman spectrum fitted by Farell and Iyengar (1999) to the measured turbulence power spectra at $z/\delta = 0.5$.

2.3. Calculation of Wind Load Coefficients

Force measurements on the model heliostat were taken using four three-axis load cells, mounted on a rotary turntable in Figure 1. Each load cell has a capacity of 500 N with a sampling frequency of 1 kHz in all three axes and an accuracy of ±0.5% of full scale. The heliostat was modelled as a thin flat plate in the absence of a support structure. A series of six square aluminium plates with 3 mm thickness and chord length (c) ranging from 300 mm to 800 mm were manufactured and mounted on a common pylon with a telescopic design to allow the heliostat elevation axis height H to vary between 0.35 m and 0.6 m. The peak drag and lift forces on the plate (D and L in Figure 1) were determined using the three-sigma approach from the difference between the measured forces on the heliostat (plate mounted to pylon) and those on the heliostat pylon in the absence of a mounted plate. The peak hinge and overturning moments (M_{Hy} and M_y in Figure 1) were calculated from the product of the forces on the plate and the longitudinal and vertical distances from the centre of pressure to the centre of the plate, respectively. In order to normalise the loads with respect to the heliostat size, the peak wind load coefficients on the plate were calculated following Peterka and Derickson (1992) as:

$$c_D = \frac{D}{1/2\rho\bar{U}^2 A} \tag{1}$$

$$c_L = \frac{L}{1/2\rho\bar{U}^2 A} \tag{2}$$

$$c_{M_{Hy}} = \frac{M_{Hy}}{1/2\rho\bar{U}^2 Ac} \tag{3}$$

$$c_{M_y} = \frac{M_y}{1/2\rho\bar{U}^2 AH} \tag{4}$$

Here ρ (kg/m^3) is the density of air, $\bar{U}$ (m/s) is the mean wind speed at the heliostat elevation axis height H, $A = c^2$ (m^2) is the area of the square heliostat mirror of chord length c.

3. Results and Discussion

3.1. Peak Wind Loads on an Isolated Heliostat in Stow Position

3.1.1. Effect of Heliostat Chord Length and Elevation Axis Height

Figure 4 shows the effect of the heliostat chord length on the peak wind load coefficients on an isolated heliostat in stow position exposed to SR1 and SR2. The peak lift coefficients for SR2 in Figure 4(a) and the peak hinge moment coefficients in Figure 4(b) are approximately double those for SR1. Both the peak lift and peak hinge moment coefficients increase by approximately double as the chord length is halved from 0.8 m to 0.4 m. This indicates that there is an inverse proportionality between the wind load coefficients and the chord length of the heliostat mirror.

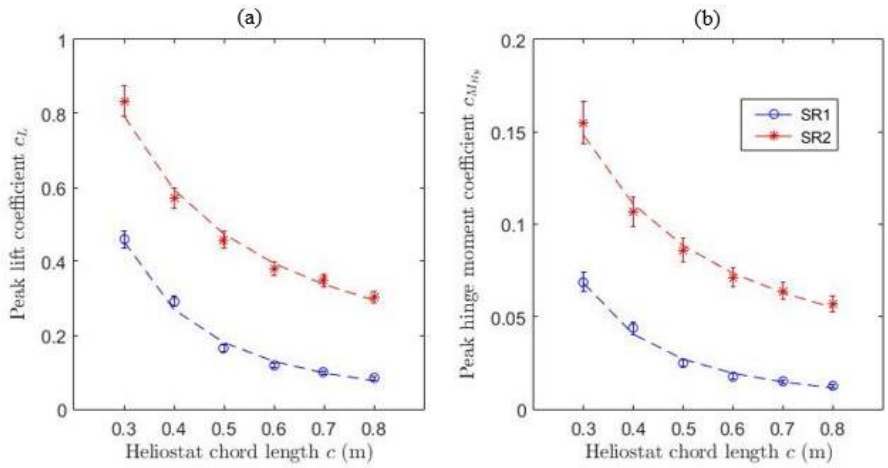

Figure 4. Effect of heliostat chord length *c* for SR1 and SR2 on: (a) peak lift coefficient; (b) peak hinge moment coefficient on an isolated heliostat in stow position.

Figure 5 presents the peak lift coefficient c_L and peak hinge moment coefficient $c_{M_{Hy}}$ as a function of the ratio of elevation axis height to chord length H/c at three different heights, non-dimensionalised with the ABL thickness H/δ generated by SR2. The effect of increasing the height at which the heliostat mirror is stowed in the ABL, H/δ, from 0.3 to 0.5 results in a vertical shift of peak c_L and peak $c_{M_{Hy}}$ to larger magnitudes at constant H/c. Conventional heliostats are commonly designed for the ratio H/c of 0.5 (Téllez *et al.* 2014), however $H/c \approx$ 0.7 for a heliostat with a horizontal primary axis. Reductions of approximately 50% in c_L and 40% in $c_{M_{Hy}}$ are possible by lowering H/c from 0.7 to 0.5 for a heliostat without a horizontal primary axis. Hence, the overall mass and strength of the heliostat can be reduced as the length of the pylon required is shorter. Designing for the smaller H/c of 0.5 can therefore lead to savings in the cost of manufacturing and installation of the heliostat (Emes *et al.* 2017).

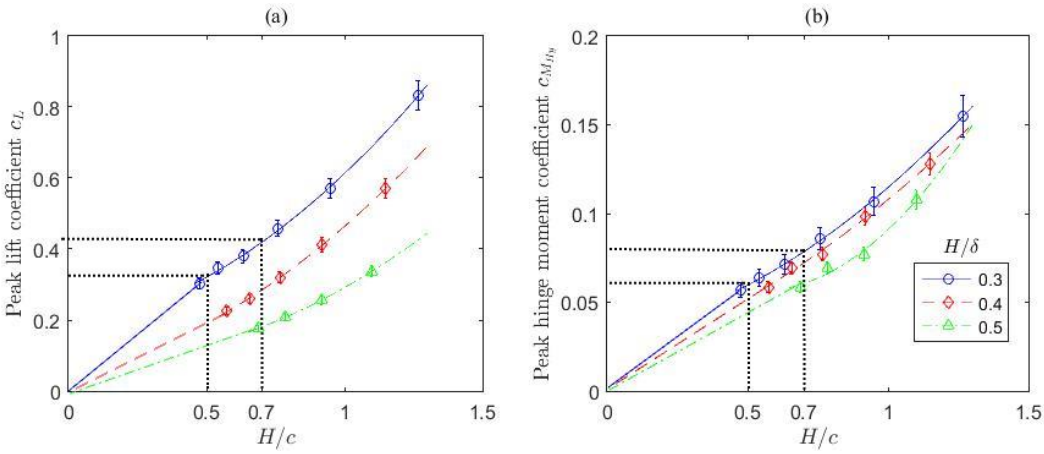

Figure 5. Effect of the ratio of heliostat elevation axis height to chord length H/c for SR2 on: (a) peak lift coefficient; (b) peak hinge moment coefficient on an isolated heliostat in stow position (Emes *et al.* 2017).

3.1.2. Effect of Approaching Turbulence Characteristics

Figure 6 shows the effect of the ratio of longitudinal integral length scale to heliostat chord length L_u^x/c at a constant longitudinal turbulence intensity I_u on the peak wind load coefficients on a stowed heliostat. At each turbulence intensity, the peak lift coefficient (Figure 6(a)) and peak hinge moment coefficient (Figure 6(b)) on the heliostat increase linearly with increasing L_u^x/c from 2 to 8. In addition, the pronounced linear increase of the peak wind load coefficients on stowed heliostats at turbulence intensities larger than 10% in the current study is in agreement with a similar finding by Peterka *et al.* (1989) for the peak drag and lift coefficients on heliostats in operating positions. Hence, the peak wind loads on an isolated heliostat in stow position can be significantly reduced by lowering the value of L_u^x/c. This can be achieved by lowering the stow height and thus decrease L_u^x approaching a stowed heliostat with constant c, such as using a telescopic pylon design. Alternatively, H/c could be reduced to less than 0.5 by manufacturing heliostat mirrors with larger c at a constant elevation axis height H and thus constant I_u.

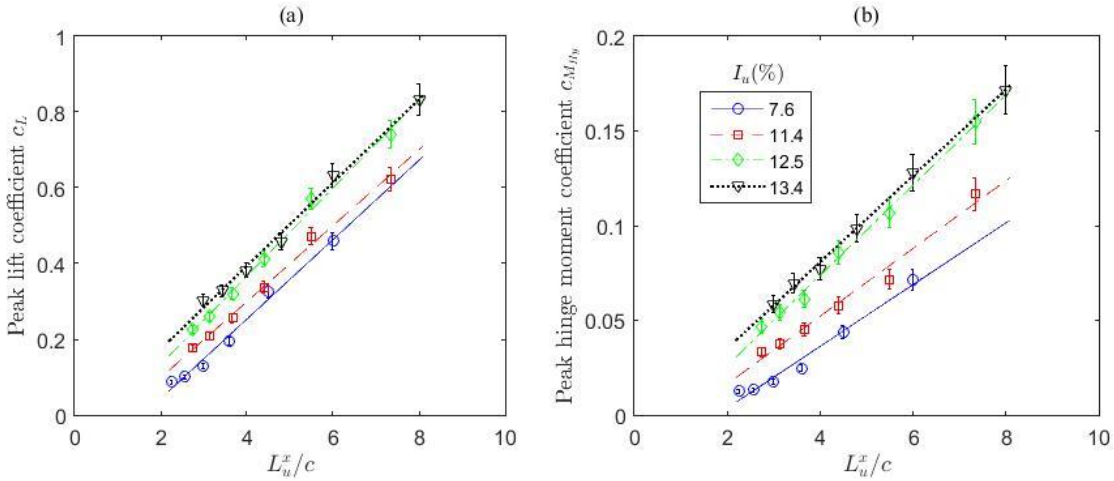

Figure 6. Effect of length-scale-to-chord ratio L_u^x/c at constant turbulence intensities I_u on: (a) peak lift coefficient; (b) peak hinge moment coefficient on a stowed heliostat.

3.2. Peak Wind Loads on an Isolated Heliostat in Operating Positions

3.2.1. Effect of Approaching Turbulence Characteristics

Figure 7 presents the mean and peak drag coefficients for two flow configurations: a uniform, smooth flow with a turbulence intensity (I_u) of 2%, and the ABL generated by SR1 with an average I_u of 8% at the mid-point of the heliostat facet in the normal position ($\alpha = 90°$). Comparisons of the effects between the two flow profiles show an increase of up to 1.28 times in peak drag load at the highest elevation angle when turbulence intensity is increased from 2% to 8%. The substantial increase in peak drag coefficient is not reflected in the mean drag coefficient, although it increased by 5% at elevation angles above 45°. The relative differences between mean and peak loads at each flow condition suggests that turbulence intensity has the

greatest effect on peak drag load, but a minor effect on mean drag load. This is consistent with the definition of turbulence intensity where higher temporal fluctuations in velocity corresponds to a larger turbulence intensity value. The result reinforces previous findings that turbulent flow can cause increased drag loads on heliostats at operating positions, although it does not address discrepancies found in studies by Peterka *et al.* (1989) and Pfahl *et al.* (2011) that used similar experimental flow conditions. Since these studies also used spires to generate turbulence with large longitudinal integral length scales, it is hypothesised that spatial fluctuations in velocity are not captured in the consideration of turbulence intensity. Therefore, it is possible that the presence of different integral length scales may also have an effect on drag loads.

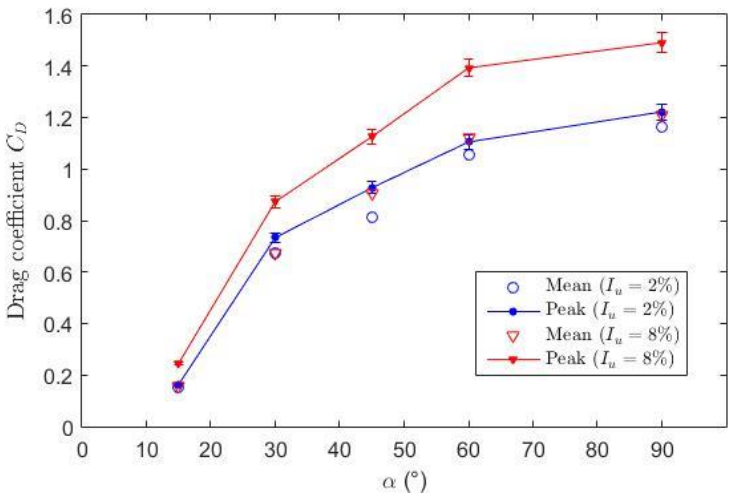

Figure 7. Effect of turbulence intensity I_u in a simulated ABL on the mean and peak drag coefficients at different elevation angles (α).

3.2.2. Effect of Heliostat Elevation (α) and Azimuth (β) Angles

Figure 8 shows the peak drag coefficients, measured on a heliostat with a facet chord length c of 800mm, as a function of elevation angle α and azimuth angle β, exposed to the simulated ABL generated by SR1. At $\beta = 0°$, the heliostat facet is positioned directly in-line with the incident flow. The results show the expected increase in drag loads as elevation angle increases, and a decrease in drag load with increasing azimuth angle, both of which relate directly to the projected area of the facet exposed to the incident wind flow. At $\beta = 135°$ and 180°, the heliostat facet is facing the opposite direction to the incident wind flow. At these positions, wind interacts with the support pylon prior to the facet, and elevation angles result in rotations that are opposite to when the windward surface of the facet is incident to the flow. Comparisons of $\beta = 135°$ and 180° with their counterparts at $\beta = 45°$ and 90° show that the peak drag loads on the heliostat are smaller at $15° \leq \alpha \leq 90°$. The lowest drag loads occur at $\alpha = 15°$ due to the streamline position of the facet, whereas at $\alpha = 90°$ the large facet area limits the impact of the pylon on load reduction. At other elevation angles however, a reduction of up to 30% in the peak drag loads is observed, which indicates that the support structure has a mitigating effect on the drag loads on an isolated heliostat during operation. In addition, the overall highest drag

load at all elevation angles is when $\beta = 0^o$, showing that for an isolated heliostat at operating positions, the worst-case aerodynamic load occurs when the heliostat is directly in-line with the incident flow.

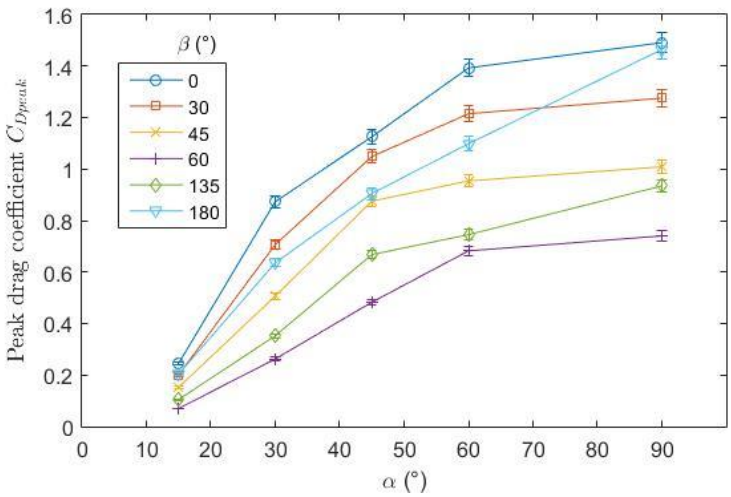

Figure 8. The effect of heliostat elevation α and azimuth β angles on the peak drag coefficient for a heliostat in operation.

4. Conclusions

Calculated peak wind load coefficients on an isolated heliostat in stow position showed an inverse proportionality with the chord length of the heliostat mirror, which suggests that the coefficients could be optimised by increasing the size of the heliostat mirror relative to the sizes of the relevant eddies approaching the heliostat. The peak lift and hinge moment coefficients on a stowed heliostat could be reduced by as much as 40% by lowering the ratio of elevation axis height to chord length of the heliostat mirror, H/c, to less than 0.5. A significant linear increase of the peak wind load coefficients occurred at longitudinal turbulence intensities I_u greater than 10% and with increasing length-scale-to-chord ratio L_u^x/c in the simulated ABL. Hence, the critical scaling parameters of the heliostat should be carefully considered depending on the turbulence characteristics of the site. For heliostats in operating positions, a similar increase in the peak drag coefficients was observed at higher turbulence intensities, although the effect on mean drag loads were significantly less. Peak wind loads on operating heliostats exposed to $I_u = 8\%$ at all of the elevation angles tested were highest when the facet was directly in-line with the incident flow at an azimuth angle β of 0°. However, a reduction in the peak drag coefficient was found at $\beta > 90°$ due to the interference of the support structure when the wind approaches from the back of the operating heliostat mirror. The results show that the wind loads on isolated heliostats in stow and operating positions are highly sensitive to the boundary layer characteristics, including the turbulence intensity and the ratio of the integral length scale to the heliostat chord length. Optimisation of the heliostat mirror chord length and elevation axis height to the characteristics of the approaching turbulence can significantly reduce the design wind loads and thus the cost of manufacturing the heliostat components.

References

Banks, D., 2011. 'Measuring peak wind loads on solar power assemblies', in: 13th International Conference on Wind Engineering, Amsterdam, Netherlands.

Cook, N.J., 1978, 'Determination of the model scale factor in wind-tunnel simulations of the adiabatic atmospheric boundary layer', *Journal of Wind Engineering and Industrial Aerodynamics*, 2, p311-321.

Counihan, J., 1973, 'Simulation of an adiabatic urban boundary layer in a wind tunnel', *Atmospheric Environment*, 7, p673-689.

Coventry, J., Campbell, J., Xue, Y.P., Hall, C., Kim, J.-S., Pye, J., Burgess, G., Lewis, D., Nathan, G. and Arjomandi, M., 2013, 'Heliostat Cost Down Scoping Study–Final Report', STG-3261 Rev 01; ANU, Canberra.

Coventry, J. and Pye, J., 2014, 'Heliostat cost reduction–where to now?', *Energy Procedia*, 49, p60-70.

De Bortoli, M., Natalini, B., Paluch, M. and Natalini, M., 2002, 'Part-depth wind tunnel simulations of the atmospheric boundary layer', *Journal of Wind Engineering and Industrial Aerodynamics*, 90, p281-291.

Emes, M.J., Arjomandi, M., Ghanadi, F. and Kelso, R.M., 2017, 'Effect of turbulence characteristics in the atmospheric surface layer on the peak wind loads on heliostats in stow position', *Solar Energy*, 157, p284-297.

Emes, M.J., Arjomandi, M. and Nathan, G.J., 2015, 'Effect of heliostat design wind speed on the levelised cost of electricity from concentrating solar thermal power tower plants', *Solar Energy*, 115, p441-451.

ESDU 85020 (1985), Characteristics of atmospheric turbulence near the ground - Part II: single point data for strong winds (neutral atmosphere), Engineering Sciences Data Unit, London, UK.

Farell, C. and Iyengar, A.K., 1999, 'Experiments on the wind tunnel simulation of atmospheric boundary layers', *Journal of Wind Engineering and Industrial Aerodynamics*, 79, p11-35.

Hernández-Moro, J. and Martínez-Duart, J.M., 2012, 'CSP electricity cost evolution and grid parities based on the IEA roadmaps', *Energy Policy*, 41, p184-192.

Hinkley, J.T., Hayward, J.A., Curtin, B., Wonhas, A., Boyd, R., Grima, C., Tadros, A., Hall, R. and Naicker, K., 2013, 'An analysis of the costs and opportunities for concentrating solar power in Australia', *Renewable Energy*, 57, p653-661.

IEA-ETSAP and IRENA (2013), *Concentrating Solar Power Technology Brief*.

IRENA, 2013, 'Renewable Power Generation Costs in 2012: An Overview', Bonn, Germany.

IRENA, 2015, 'The Power to Change: Solar and Wind Cost Reduction Potential to 2025', Bonn, Germany.

Irwin, H., 1981, 'The design of spires for wind simulation', *Journal of Wind Engineering and Industrial Aerodynamics*, 7, p361-366.

Kolb, G.J., Ho, C.K., Mancini, T.R. and Gary, J.A., 2011, 'Power Tower Technology Roadmap and Cost Reduction Plan', SAND2011-2419; Sandia National Laboratories, Albuquerque, USA.

Kolb, G.J., Jones, S.A., Donnelly, M.W., Gorman, D., Thomas, R., Davenport, R. and Lumia, R., 2007, 'Heliostat Cost Reduction Study', SAND2007-3293; Sandia National Laboratories, Albuquerque, USA.

Mehos, M., Turchi, C., Jorgenson, J., Denholm, P., Ho, C. and Armijo, K., 2016, 'On the Path to SunShot. Advancing Concentrating Solar Power Technology, Performance, and Dispatchability', National Renewable Energy Laboratory (NREL), Golden, Colorado, USA.

Mehos, M., Turchi, C., Vidal, J., Wagner, M., Ma, Z., Ho, C., Kolb, W., Andraka, C. and Kruizenga, A., 2017, 'Concentrating Solar Power Gen3 Demonstration Roadmap', National Renewable Energy Laboratory (NREL), Golden, Colorado, USA.

Peterka, J.A. and Derickson, R.G., 1992, 'Wind load design methods for ground-based heliostats and parabolic dish collectors', SAND92-7009; Sandia National Laboratories, Albuquerque, USA.

Peterka, J.A., Tan, Z., Cermak, J.E. and Bienkiewicz, B., 1989, 'Mean and peak wind loads on heliostats', *Journal of solar energy engineering*, 111, p158-164.

Pfahl, A., Buselmeier, M. and Zaschke, M., 2011, 'Wind loads on heliostats and photovoltaic trackers of various aspect ratios', *Solar Energy*, 85, p2185-2201.

Pfahl, A., Coventry, J., Röger, M., Wolfertstetter, F., Vásquez-Arango, J.F., Gross, F., Arjomandi, M., Schwarzbözl, P., Geiger, M. and Liedke, P., 2017a, 'Progress in heliostat development', *Solar Energy*, 152, p3-37.

Pfahl, A., Gross, F., Liedke, P., Hertel, J., Rheinländer, J., Mehta, S., Vásquez-Arango, J.F., Giuliano, S. and Buck, R., 2017b, 'Reduced to Minimum Cost: Lay-Down Heliostat with Monolithic Mirror-Panel and Closed Loop Control'. In: *Proc., SolarPACES 2017*, Santiago, Chile.

Pfahl, A., Randt, M., Meier, F., Zaschke, M., Geurts, C. and Buselmeier, M., 2015, 'A holistic approach for low cost heliostat fields', *Energy Procedia*, 69, p178-187.

Téllez, F., Burisch, M., Villasente, Sánchez, M., Sansom, C., Kirby, P., Turner, P., Caliot, C., Ferriere, A., Bonanos, C.A., Papanicolas, C., Montenon, A., Monterreal, R. and Fernández, J., 2014, 'State of the Art in Heliostats and Definition of Specifications', 609837; STAGE-STE Project, Madrid, Spain.

Acknowledgements

Support for the work has been provided by the Australian Government Research Training Program Scholarship and by the Australian Solar Thermal Research Initiative (ASTRI) through funding provided by the Australian Renewable Energy Agency (ARENA).